Bio-Design and Manufacturing (2025) 8:609–624
https://doi.org/10.1631/bdm.2400341

RESEARCH ARTICLE

Homologous cancer cell membrane-camouflaged natural pH-sensitive chalk for enhanced drug targeting delivery in hepatocellular carcinoma

Yangbo Zhu[1] · Pengfei Cui[4] · Lijuan Zhao[2,3] · Qi Ling[1] · Jiayi Qin[2,3]

Received: 25 August 2024 / Accepted: 3 March 2025

Abstract

The therapeutic efficacy of hepatocellular carcinoma (HCC) medication is severely compromised by inadequate drug delivery to tumor sites. Herein, we fabricated a biomimetic nanoplatform for improved drug targeting ability by wrapping H22 tumor cell membranes around natural chalk to encapsulate the model drug doxorubicin (C-DOX@H22 CM). When camouflaged with H22 tumor cell membranes, C-DOX@H22 CM achieved primary targeting to the tumor tissues due to the immune escape ability and secondary deep targeting to HCC cells owing to the homologous targeting properties. The cellular uptake of C-DOX@H22 CM by H22 cells was via clathrin-mediated endocytosis. Meanwhile, C-DOX@H22 CM exhibited the property of deep penetration into dense tumor tissues. Moreover, the pH-responsive characteristics of the natural chalk enabled C-DOX@H22 CM to achieve endosomal escape and drug release, thereby expanding its antitumor effects without compromising biocompatibility. Importantly, the in vivo experiments also confirmed that C-DOX@H22 CM had favorable antitumor efficacy and biosafety in the H22 tumor-bearing mouse model. Overall, the novel C-DOX@H22 CM nanoplatform provides a safe and effective treatment option for HCC and has the potential to achieve clinical translation for the targeted delivery of other drugs for the treatment of various tumors.

✉ Qi Ling
lingqi@zju.edu.cn

✉ Jiayi Qin
jiayiqin@zju.edu.cn

[1] Division of Hepatobiliary and Pancreatic Surgery, Department of Surgery, The First Affiliated Hospital, Zhejiang University School of Medicine, Hangzhou 310003, China

[2] Department of Clinical Pharmacy, The First Affiliated Hospital, Zhejiang University School of Medicine, Hangzhou 310003, China

[3] Zhejiang Provincial Key Laboratory for Drug Evaluation and Clinical Research, Hangzhou 310003, China

[4] School of Pharmacy, Changzhou University, Changzhou 213164, China

Graphical abstract

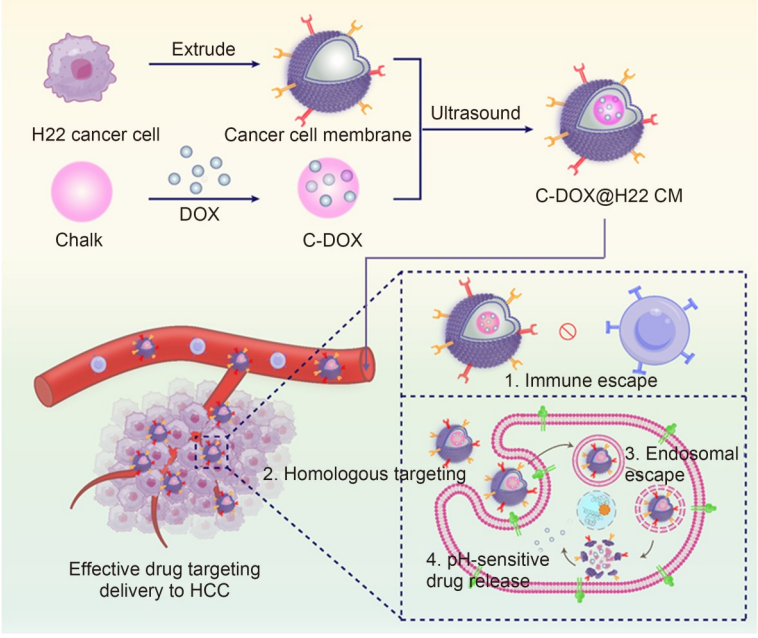

Keywords Biomimetic drug delivery system · Tumor cell membrane · pH-sensitive · Chalk · Hepatocellular carcinoma

1 Introduction

Liver cancer is the sixth most prevalent cancer worldwide, with approximately 760 000 deaths reported in 2022 [1]. Hepatocellular carcinoma (HCC) is the most common form of primary liver cancer, accounting for 75%–85% of all cases. Most HCC patients are diagnosed at the advanced stage, when effective surgical resection is usually no longer possible. These unresectable HCC patients are treated with interventional therapy, liver transplantation, and/or medical therapy [2–4]. Although conventional drugs are available, the clinical efficacy of these medications is low and the side effects are severe due to their insufficient exposure to tumor cells and excessive accumulation in normal tissues. Thus, it is imperative to explore more effective and safer strategies for the targeted delivery of therapeutic agents to tumors.

With the development of nanotechnology, nanodrug delivery systems have exhibited enhanced therapeutic efficacy to overcome the drawbacks related to conventional therapy [5–8]. Notably, several nanodrugs (doxorubicin liposomes, paclitaxel albumin, etc.) have been used clinically [9, 10]. Nevertheless, many nanomedicines are rapidly cleared by the immune system in the circulation, do not effectively target pathological sites through passive targeting [11], and therefore do not achieve improvements in progression-free survival or overall survival at an overall level. To address these obstacles, the functionalization of nanoparticles (NPs) with specific ligands, such as folic acid, peptides, transferrin, aptamers, and antibodies, has been reviewed [12]. However, even though numerous nano-formulations with active targeting functions have been reported, their selectivity to tumor tissues remains inadequate due to the stimulation of plasma protein opsonization [13] and the ability to add multiple functionalities using additional materials is often accompanied by increased preparation steps and costs at the expense of biocompatibility [14, 15]. The efficacy of tumor-targeted therapy is still strongly restricted by its unfavorable intracellular drug release, especially being trapped in endo-lysosomes [16]. Due to the above deficiencies, it remains challenging to improve the targeting and endosomal escape capabilities and biocompatibility of NPs.

Recently, the emergence of cell membrane camouflage techniques has brought novel insight into tumor-targeted drug delivery, attributed to their high targeting ability and low immunogenicity [17–19]. Natural cell membranes equip the NPs with the inherent features of the source cells without affecting their physicochemical properties [20]. To date, various biomimetic NPs modified by natural cell membranes have been reported, such as erythrocyte membrane-coated NPs, which exhibit long-term circulation [21], macrophage membrane-camouflaged NPs, which exhibit immunological escape [22], NPs with inflammatory targeting capability in the

brain [23], NPs that target orthotopic rectal cancer cells [24], hybrid *Staphylococcus aureus* and *Veillonella atypica* cell membranes engineered microrobots with inflammatory and anaerobic targeting [25], and hybrid cell membrane-modified nanomotors with homologous tumor-targeting capability and enhanced ability to bypass the blood–brain barrier (BBB) [26], and cancer cell membrane-coated NPs that exhibit long circulation time and active tumor cell targeting [27] or enhanced stability and antitumor immune activity [28]. Among them, tumor cell membranes have been a research hotspot in recent years [28]. Driven by the unique molecules expressed on the tumor cell membranes (adhesion proteins, cluster of differentiation 47 (CD47), etc.), they have homologous targeting function and immune escape ability, thereby enhancing drug intracellular accumulation [29, 30]. More remarkably, they can be easily obtained and mass-produced through in vitro simple cell proliferation and membrane extraction [31]. Calcium carbonate ($CaCO_3$), as a nontoxic biomineral, has attracted great attention for biomedical applications due to its high drug-loading capacity, outstanding biocompatibility, inherent pH sensitivity, and low cost [32–34]. $CaCO_3$ is structurally stable under physiological conditions, readily generates carbon dioxide (CO_2), and achieves rapid volume expansion under acidic conditions, making $CaCO_3$ a promising candidate for promoting endosomal escape and triggering the release of cargo [35]. In addition, previous studies have shown that calcium carbonate can be used for acidification to increase the intracellular alkalization pH, thereby enhancing the antitumor efficacy of weak-base chemotherapeutic drugs [36]. Unfortunately, many studies found that there was no better way to separate the suspended nanoscale calcium carbonate in water [37]. In particular, chalk is an inert natural biomineral mainly composed of stable $CaCO_3$ (biogenic calcite) [38], and our previous research demonstrated that chalk possessed superior absorption and antitumor effects [39].

Herein, we constructed a biomimetic tumor cell membrane-coated chalk that showed promoted effectiveness against HCC and negligible side effects. As shown in Scheme 1, the chemotherapeutic drug doxorubicin (DOX) was selected as the model drug and adsorbed onto the chalk (C-DOX). Subsequently, an H22 cell membrane was wrapped around the DOX-adsorbed chalk to encapsulate the C-DOX (C-DOX@H22 CM). The preparation process of C-DOX@H22 CM was simple. C-DOX@H22 CM could avoid being captured by immune cells to achieve primary targeting to the tumor tissues due to the stealth coating of H22 tumor cell membrane (H22 CM) and secondary active targeting to HCC cells owing to the excellent homing effects of the tumor cell membranes. Once C-DOX@H22 CM was taken up by HCC cells, the lower pH accelerated the decomposition of the NPs, leading to the destruction of the lysosome, followed by the release of DOX, thus amplifying the cancer therapy. In this study, we assessed the tumor targeting efficiency and antitumor effect of C-DOX@H22 CM compared with erythrocyte membrane-coated NPs or normal NPs in immune or tumor cell lines and H22 subcutaneous tumor models. In addition, the biosafety of C-DOX@H22 CM was evaluated. Overall, the natural C-DOX@H22 CM nanoplatform may provide an attractive paradigm for effective drug targeting of liver tumor cells while avoiding its adverse effects, which might inspire a new concept for future translational research on the treatment of HCC.

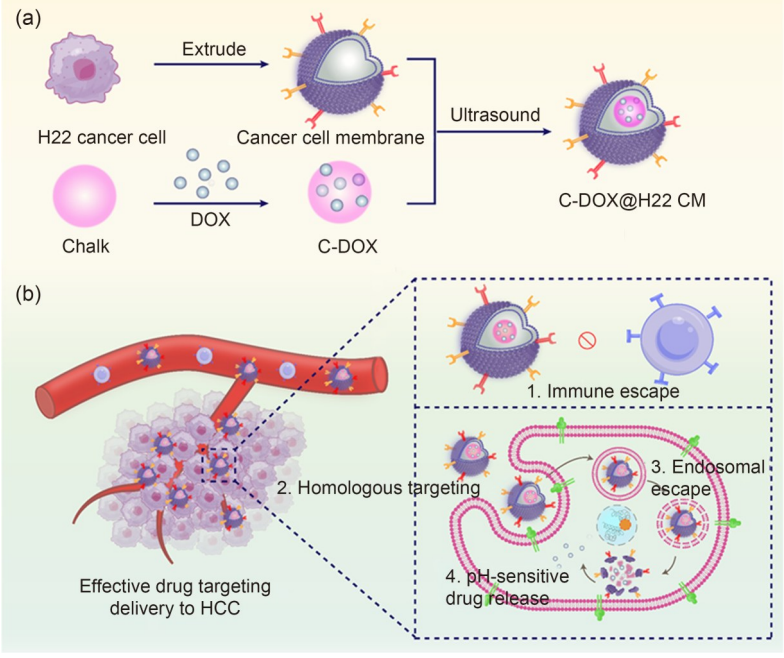

Scheme 1 Schematic illustration for the construction process of C-DOX@H22 CM (a) and effective drug targeting to HCC (b)

2 Materials and methods

2.1 Materials

Dulbecco's modified Eagle's medium (DMEM), Roswell Park Memorial Institute (RPMI) 1640 medium, fetal bovine serum (FBS), dimethyl sulfoxide (DMSO), sodium dodecyl sulfate-polyacrylamide gel electrophoresis (SDS-PAGE) Bis-Tris precast gel, protein loading buffer, poly-D-lysine (PDL), 4',6-diamidino-2-phenylindole (DAPI), amiloride hydrochloride, and doxorubicin hydrochloric acid (DOX·HCl) were provided by Shanghai Titan Technology Co., Ltd. (China). The chalk was purchased from Xincheng Mineral Products Co., Ltd. (Hebei, China). Phosphate-buffered saline (PBS), hematoxylin-eosin (H&E) high-definition (HD) constant dye kit, terminal deoxynucleotidyl transferase-mediated dUTP nick-end labeling (TUNEL) assay kit, Ki67 antibody, CY3-labeled goat anti-rabbit immunoglobulin G (IgG), protein marker, 3,3'-dioctadecyloxacarbocyanine perchlorate (DiO), and fluorescein isothiocyanate (FITC) fluorescent dyes were purchased from Wuhan Service Technology Co., Ltd. (China). The cell membrane protein and cytoplasm protein extraction kit, phenylmethylsulfonyl fluoride (PMSF), and Fast Silver Stain Kit were obtained from Beyotime (China). Nystatin was purchased from Dalian Meilun Biotechnology Co., Ltd. (China). Chlorpromazine was purchased from TCI Chemical Trading Co., Ltd. (Shanghai, China). All materials were of analytical grade and without purification unless otherwise stated.

2.2 Cell culture and animals

HCC cells (H22) were provided by Wuhan Service Technology Co., Ltd. Macrophage leukemia cells (RAW264.7), colon cancer cells (CT26), and embryonic fibroblasts (NIH-3T3) were obtained from the Shanghai Academy of Sciences (China). The cells were cultured in RPMI 1640 or DMEM medium containing 10% FBS and 1% antibody in a 37 °C, 5% CO_2 incubator.

Female BALB/c mice (6–8 weeks old, approximately 20 g) were selected for the animal experiments. To establish the HCC model, 1×10^6 H22 cells were subcutaneously inoculated into the right legs of the mice. All reagents and consumables were sterilized before use.

2.3 Extraction and protein characterization of cell membranes

Tumor cell membranes were extracted from H22 cells using a cell membrane protein and cytoplasm protein extraction kit. Briefly, 30 million H22 cells were collected and resuspended in a pre-cooled lysing buffer with PMSF. Subsequently, the cell homogenate was transferred to an ice bath for 15 min after centrifugation at 4 °C and 600*g* for 5 min. The obtained cells were subjected to the freeze–thaw experiment at least five times, followed by collection of the supernatant by centrifugation at 4 °C and 700*g* for 10 min. The cell membranes were extracted by centrifugation at 4 °C and 14 000*g* for 30 min, then lyophilized, and stored at −80 °C for the subsequent experiments. Finally, H22 tumor cell membrane vesicles (H22 CM) were obtained through 400 nm polycarbonate films with an Avanti micro extruder (Avanti Polar Lipids, USA).

Red blood cell (RBC) membranes were extracted using hypotonic treatment as previously reported [40]. Briefly, fresh heparinized blood was withdrawn from the BALB/c mice. Buffy coats and plasma were removed after centrifugation at 4 °C and 3000 r/min for 10 min. The RBCs were washed with five volumes of ice-cold PBS, and the precipitate was collected after centrifugation at 4 °C and 800*g* for 5 min. The RBCs were resuspended in a cold hypotonic solution (0.25× PBS) for 20 min and subsequently centrifuged at 4 °C and 800*g* for 5 min. After removing the hemoglobin, the RBC membranes (RBCMs) were collected via centrifugation at 4 °C and 800*g* for 5 min and purified with PBS solution. After sonicating for 30 min at 100 W, the final cell membrane-derived vesicles were obtained through a liposome extruder with 400 nm polycarbonate track-etch (PCTE) membrane.

2.4 Preparation and characterization of C-DOX@H22 CM

C-DOX@H22 CM was prepared via the ultrasound method. A mixture of chalk (10 mg) and DOX (1 mg) was dissolved in deionized water and stirred for 12 h. The precipitate was collected to obtain the C-DOX core after centrifugation at 8000 r/min for 3 min. Next, 250 μg H22 CM and C-DOX (mass ratio=1:1) were mixed well and sonicated with gradient programs (50 W, 15 min, 3 s, 3 s) to construct C-DOX@H22 CM. The C-DOX@RBCM was prepared following the procedure described above, except that the cell membranes were extracted from the RBCs. The fluorescence spectrophotometer FS5 (Edinburgh Instruments, UK) was used to measure the emission curves of DOX, C-DOX, and C-DOX@H22 CM at an excitation wavelength (λ_{Ex}) of 490 nm, and the fluorescence intensity of DOX in the supernatant was used to calculate the encapsulation efficiency (Fig. S2 in the supplementary information) and loading rate. The ultraviolet–visible (UV–Vis) absorption spectra of C-DOX@H22 CM were measured using a UV–Vis spectrophotometer (UV-1900; Shimadzu, Japan) to determine the intermolecular forces in the NPs after mixing with 0.2% sodium dodecyl sulfate (SDS) solution. Fourier transform infrared (FTIR) spectroscopy (FTIR-IS50; Thermo Fisher, USA) was employed to determine the possible interactions

between the drug, chalk, and surface membrane coating, with the wavelength scanning from 400 to 4000 cm^{-1}. The particle size and zeta potential of the surface charge were measured by a dynamic light scattering instrument (Zetasizer Nano; Malvern, UK), and the surface structures of H22 CM, chalk, and C-DOX@H22 CM were observed under a transmission electron microscope (TEM Tecnai G20; FEI, USA). Cell membrane proteins were characterized by SDS-PAGE according to the protocol previously reported by Ying et al. [41] to confirm the successful encapsulation of H22 CM on the C-DOX. Samples preprocessed in the loading buffer and protein markers were added to the gel wells. Electrophoresis was carried out at 100 V for 110 min. The gel was stained with Silver staining solution for 30 min and then decolored on a shaker overnight for photographic analysis. Cell membrane fragments of C-DOX@H22 CM were then assessed by Western blot. To further visualize the cell membrane coating on C-DOX, H22 CM was stained with a fluorescent DiO probe. Briefly, the H22 CM and DiO staining working solutions were incubated at 37 °C in the dark. After staining for 30 min, the supernatant containing the unstained fluorescent probe was removed by centrifugation at 14 000*g* for 30 min at 4 °C. Then the precipitate was finally collected for the preparation of C-DOX@CM-DiO. C-DOX@CM-DiO was prepared in a similar manner to the preparation method for C-DOX@CM. In brief, 10 μL samples were dropped onto a glass slide, and covered, and the green fluorescence (DiO) and red fluorescence (DOX) were observed under bright-field confocal laser scanning microscopy (CLSM, Nikon, Japan).

2.5 pH-sensitive in vitro drug release

The dialysis method was applied to calculate the cumulative release of DOX in C-DOX@CM under an acidic environment. Each group was laid in a dialysis bag (molecular weight cut-off (MWCO): 3500) and immersed in 15 mL PBS (pH: 7.4, 4.5). At a predetermined time point, 3 mL of release solution was collected and supplied with an equal volume of fresh PBS. The concentration of released DOX was further detected using a fluorescence spectrophotometer (λ_{Ex}= 490 nm, λ_{Em}=590 nm, with λ_{Em} representing the emission wavelength) (FS5; Edinburgh Instruments).

2.6 In vitro cytotoxicity assay and safety evaluation

The in vitro cytotoxicity of the nanoparticles was evaluated in H22 and NIH-3T3 cells via MTT assay. In brief, the cells were seeded in 96-well plates and then treated with C@H22 CM NPs (the concentration of chalk was 1, 10, 25, 50, and 100 μg/mL) and different controls. After incubation for 24 or 48 h, the supernatant was discarded, 100 μL of fresh medium containing 3-(4,5-dimethylthiazol-2-yl)-2,5-diphenyltetrazolium bromide (MTT, 5 mg/mL) was added, and the cells were incubated for a further 4 h. The cells were then centrifuged at 1000 r/min for 10 min; after that, the supernatant was discarded, and 150 μL of DMSO was added to each well and incubated on a shaker for 10 min. The optical density (OD) of each well at 570 nm was obtained using a microplate reader.

The hemolysis test was applied to evaluate the hemolytic effect of C-DOX@CM. First, fresh orbital blood was obtained from healthy mice into the anticoagulant tube, and then centrifuged at 4 °C, 2000 r/min for 10 min to remove the upper plasma and washed three times with pre-cold saline. The 20% erythrocyte suspension was obtained after diluting with saline. Next, the RBC suspension was incubated with various sample concentrations (0.1, 1.0, 2.5, 5.0, and 10.0 μg/mL) at 37 °C for 2 h (or with saline as the negative control and pure water as the positive control). The RBC suspensions were centrifuged at 2000 r/min for 10 min, and then the supernatants were collected for measurement of the hemoglobin OD at 540 nm. The hemolysis rate was calculated using the following formula:

$$r_h=(OD_{samples}-OD_{negative})/(OD_{positive}-OD_{negative})\times 100\%,$$

where $OD_{samples}$, $OD_{negative}$, and $OD_{positive}$ represent the optical densities of the sample, negative, and positive control groups, respectively.

2.7 In vitro cellular uptake assay

To study the homologous targeting and immune escape properties of C-DOX@H22 CM, CLSM and flow cytometry experiments were conducted. First, H22 cells were treated with DOX, C-DOX (without CM), C-DOX@RBCM (with RBC CM), and C-DOX@H22 CM (with H22 CM). Then, the cells were collected to detect the DOX fluorescence uptake by a flow cytometer (C6 Plus; BD Accuri, USA). These cells were washed with PBS and fixed in 4% paraformaldehyde for 15 min. After rinsing with PBS to discard paraformaldehyde, the cells were stained with DAPI solution for 10 min and imaged using CLSM. To explore the cellular endocytic pathway, the H22 cells were preincubated with nystatin, amiloride, or chlorpromazine for 30 min. The supernatant was removed and then replaced with C-DOX@H22 CM (DOX concentration of 2.5 μg/mL) for 4 h coculture. After washing with PBS, the cells were collected, and the fluorescence of DOX was measured by flow cytometry. Second, to ascertain the impact of cell type on cellular uptake, normal embryonic fibroblasts NIH-3T3, RAW264.7, colon cancer cells (CT26), and H22 liver cancer cells were collected after 4 h incubation with C-DOX@H22 CM (DOX concentration of 2.5 μg/mL). The DOX cellular uptake was analyzed by CLSM and flow cytometry following the

protocol mentioned above. In addition, to evaluate the competitive uptake ability of C-DOX@H22 CM, the fluorescence images were recorded as described above except that the cells were a mixture of H22 cells and NIH-3T3 cells. The tumorsphere model was established to evaluate the targeting efficiency. In brief, H22 and NIH-3T3 cells were seeded in 1.5% agarose in a 96-well plate. Next, the tumorsphere models were cocultured with DOX, C-DOX, and C-DOX@H22 CM. After 24 h of incubation, the models were placed on a coverslip and analyzed under CLSM.

2.8 In vitro antitumor assay

The in vitro antitumor effects of C-DOX@CM were assessed with H22 and NIH-3T3 cells via MTT assay. In brief, H22 or NIH-3T3 cells were seeded in a 96-well plate and incubated with DOX, C-DOX, and C-DOX@H22 CM (the final concentrations of DOX were 0.1, 1.0, 2.5, 5.0, and 10.0 μg/mL) and different controls for 24 h. Then, the supernatants were discarded and replaced with 100 μL of fresh media containing MTT (5 mg/mL) for another 4 h. After centrifugation at 1000 r/min for 10 min, the supernatant was removed. To each well, 150 μL of DMSO was added, followed by incubation for 10 min on a shaker. The OD of the samples was detected at 570 nm using a microplate reader.

2.9 In vivo targeting experiments

Indocyanine green (ICG) was chosen as the probe encapsulated in chalk, RBCM, and H22 CM-coated chalk according to the preparation method of C-DOX@H22 CM. To investigate the targeting of nanoparticles, free ICG, C-ICG, C-ICG@RBCM, and C-ICG@H22 CM (n=3) were injected via the tail vein of tumor-bearing mice when the tumor volume reached 80–100 mm^3, with a DOX content of 5 mg/kg. The tumor volume was recorded according to the following formula: length×width×width/2. Fluorescence images of the mice were recorded at 6, 24, and 48 h in an ex vivo/in vivo imaging system (ABL-X5; Tanon, China). After 48 h of injection, the mice were dissected, and the tumors and major organs (heart, liver, spleen, lungs, and kidneys) were collected and then photographed using the ex vivo/in vivo imaging system. The tumor accumulation of membrane-coated nanoparticles was studied in the H22 tumor-bearing mice. Mice were administered a single intravenous injection of C-DOX@H22 CM (5 mg/kg DOX equivalent) via the tail vein. The dissected tumors were weighed and added to a 5-mL centrifuge tube containing isopropyl alcohol (IPA) HCl 48 h after injection. After the tumors were homogenized using a high-speed disperser, the homogenate was precipitated in a thermostatic oscillator overnight and centrifuged at 13000 r/min for 15 min. The fluorescence intensity of the supernatant was measured using an FS5 fluorescence spectrometer, and the cumulative amount of DOX in the tumor was calculated using the DOX concentration-fluorescence intensity standard curve for IPA HCl (Fig. S3 in the supplementary information).

2.10 In vivo antitumor efficacy and biosafety evaluation

When the tumor volumes grew to around 80–100 mm^3, tumor-bearing mice were randomly divided into the saline, free DOX, and C-DOX@H22 CM groups (n=5). The tumor-bearing mouse models were intravenously injected with saline, free DOX, and C-DOX@H22 CM (DOX content: 5 mg/kg) every 2 d. In addition, the body weight and tumor size were recorded every day. After 9 d of injection, to assess the antitumor effects, the mice were sacrificed, and the tumor was stripped for size comparison, H&E staining, and TUNEL apoptosis detection, separately. To evaluate the potential biosafety in vivo, whole blood was collected for hepatic function and blood routine analysis, which included aspartate aminotransferase (AST), alanine aminotransferase (ALT), alkaline phosphatase (ALP), RBC, white blood cell (WBC), and platelet (PLT) quantification. The main organs were sectioned for H&E and immunofluorescence staining. Finally, the tissues were visualized under a fluorescent microscope (Nikon Eclipse C1, Japan) or CLSM.

2.11 Statistical analysis

Data were expressed as mean±standard deviation (SD). The degree of difference was analyzed by Student's t-test or one-way analysis of variance (ANOVA) using GraphPad Prism 9. The significance levels are indicated by $^{*}P<0.05$, $^{**}P<0.01$, or $^{***}P<0.001$.

3 Results and discussion

3.1 Preparation and characterization of C-DOX@H22 CM

The preparation process of the C-DOX@H22 CM is illustrated in Scheme 1. First, the H22 cell membrane was extracted from the H22 cells, and then the core chalk-loaded DOX was prepared and wrapped in the H22 membrane to form the biomimetic C-DOX@CM through the ultrasonic method. After extrusion by the liposome extruder, as shown in Fig. 1, the particle size of the H22 CM vesicles was approximately 146 nm, and the zeta potential was (−23.7±1.6) mV. The average diameter of the C-DOX@H22 CM nanoparticles increased, whereas the zeta potential was (−28.3±1.5) mV, which was similar to that of the H22 CM vesicle. DOX has the highest fluorescence characteristic peak at 590 nm under the excitation wavelength of 490 nm by the FS5

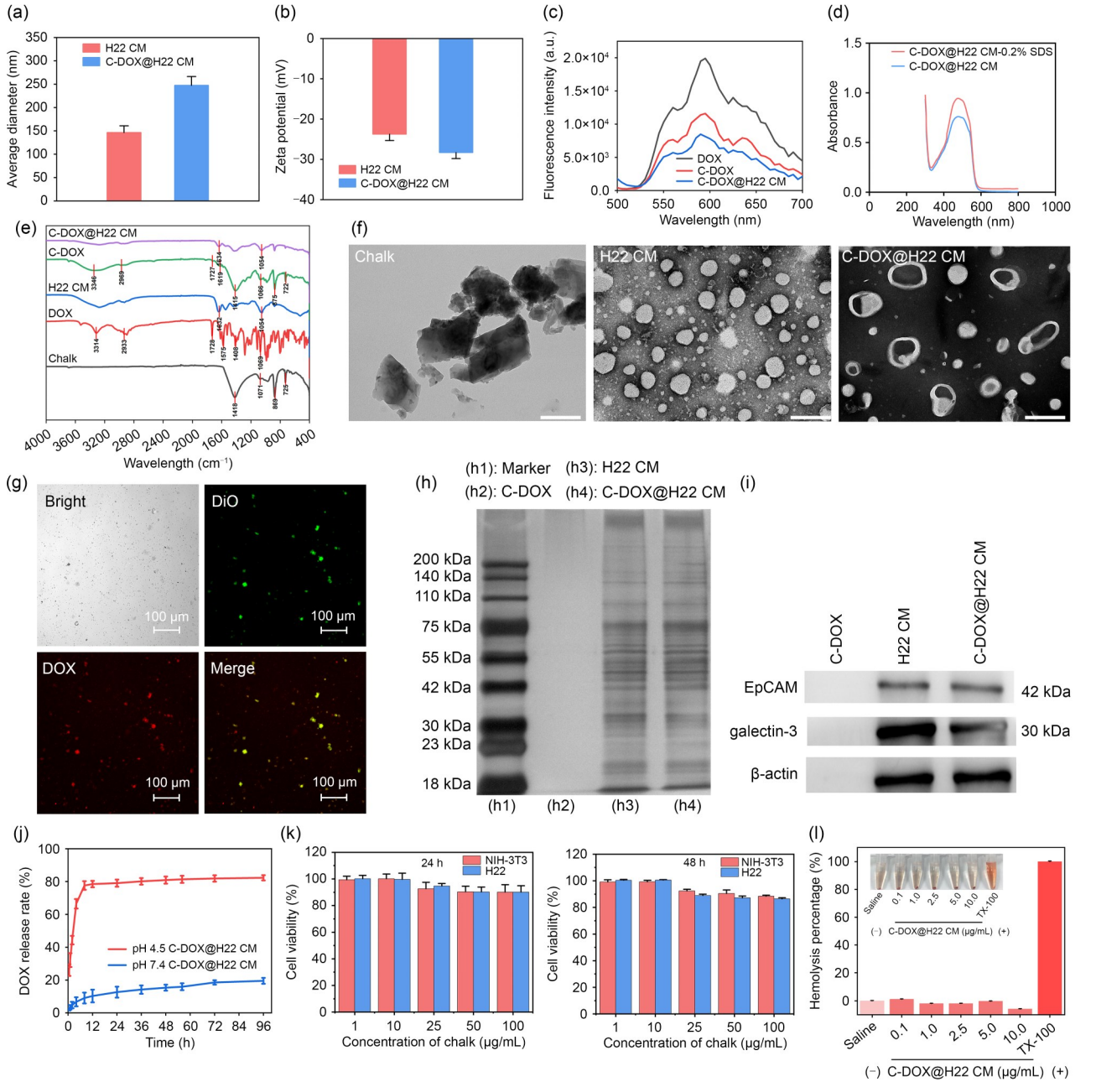

Fig. 1 Preparation and characterization of C-DOX@H22 CM. Particle size distributions (a) and zeta potential (b) of H22 CM and C-DOX@H22 CM (n=3). (c) Fluorescence spectra of DOX, C-DOX, and C-DOX@H22 CM (λ_{Ex}=490 nm, λ_{Em}=590 nm). (d) UV−Vis spectra of C-DOX@H22 CM. (e) FTIR spectra of chalk, DOX, H22 CM, C-DOX, and C-DOX@H22 CM. (f) TEM images of chalk, H22 CM, and C-DOX@H22 CM. Scale bar: 200 nm. (g) Fluorescence images of C-DOX@H22 CM. Scale bar: 100 μm. (h) Protein expression of H22 cancer cell membrane (h3) and C-DOX@H22 CM (h4) via SDS-PAGE ((h1) marker and (h2) C-DOX). (i) Expression of galectin-3 and EpCAM in C-DOX, H22 cell membrane vesicles, and C-DOX@H22 CM by Western blot analysis. (j) Release profile of C-DOX@H22 CM in PBS buffer solutions at different pH values (pH 4.5 or pH 7.4; n=3). (k) Cytotoxicity of NIH-3T3 or H22 cells after incubation with C@H22 CM NPs for 24 h and 48 h (n=6). (l) Hemolysis percentage and images of red blood cells treated with C-DOX@H22 CM at concentrations of 0.1, 1.0, 2.5, 5.0, and 10.0 μg/mL, using saline and water as negative (−) and positive (+) controls, respectively (n=3). Data are expressed as mean±standard deviation. EpCAM: epithelial cell adhesion molecule

fluorescence spectrometer. As shown in Fig. 1c, the highest peaks of C-DOX and C-DOX@H22 CM were both located at 590 nm, but the lower fluorescence values than those of DOX demonstrated that DOX was successfully encapsulated in the chalk and C-DOX was wrapped in H22 CM. In addition, as shown in Fig. 1d, the characteristic peak of DOX (around 480 nm) obviously recovered from a low, flat, broad peak to the original high, narrow peak in the UV spectra of C-DOX@H22 CM after adding 0.2% SDS, which suggested a hydrophobic interaction between C-DOX and

H22 CM. We also verified the interaction of the drug and chalk and the surface membrane wrapping of C-DOX@H22 CM by FTIR. As shown in Fig. 1e, the characteristic absorption peaks of chalk were located at 1418, 1071, 869, and 725 cm^{-1}, and the characteristic absorption peaks of DOX were located at 3314, 2933, 1728, 1575, 1408, and 1069 cm^{-1}. C-DOX basically preserved the characteristic peaks of DOX [42] and chalk [43], indicating that DOX was successfully physically adsorbed on the chalk. For C-DOX@H22 CM, a new peak around 1054 cm^{-1} was ascribed to the P=O absorption of phospholipid, and a typical peak at 1634 cm^{-1} was attributed to the C=N absorption of the amide group in H22 CM [44]. These data demonstrated the successful encapsulation of DOX on chalk and the effective coating of the cancer membranes. The TEM images (Fig. 1f) showed that H22 CM was irregularly round, with a particle size of approximately 150 nm, and the cavity of the C-DOX@H22 CM was clearly observed after negative staining, which also indirectly confirmed the successful encapsulation of CM. Subsequently, the H22 CM was stained with a DiO fluorescent probe to visualize the CM coating of C-DOX. Figure 1g shows that the green fluorescence of DiO and the red fluorescence of DOX overlapped. Taken together, these results proved that the cell membrane was successfully coated on the surface of the C-DOX NPs.

Currently, natural cell membrane-coated nanocarriers can replicate the diverse functions of membrane surface proteins from source cells onto engineered nanoparticles [45]. After Silver staining, C-DOX had no protein bands, while a common protein band of H22 CM and C-DOX@ H22 CM was observed at around 30 and 42 kDa (Fig. 1h). The results of SDS-PAGE revealed that the surface protein bands of C-DOX@H22 CM were consistent with those of H22 CM, indicating that C-DOX@H22 CM retained its cell membrane proteins. It has been reported that galectin-3 and epithelial cell adhesion molecule (EpCAM) are the main cell adhesion molecules that mediate cell adhesion to cancer cell membranes [46]. We further identified the specific membrane proteins of C-DOX@H22 CM by Western blot analysis. As shown in Fig. 1i, galectin-3 and EpCAM were enriched on the surface of the C-DOX@ H22 CM and H22 cell membranes, while the corresponding bands were rarely found on the surface of C-DOX. This indicated that C-DOX@H22 CM NPs retained cell adhesion molecules (galectin-3 and EpCAM), which can enable NPs to specifically target source tumor cells. These results confirmed that the interaction between the H22 cell membrane and C-DOX was physical adsorption. Given their unique physicochemical properties, tumor cell membranes can be considered as suitable candidates to realize drug-targeted delivery. Moreover, we measured the drug-loading and entrapment rates of C-DOX@ H22 CM. DOX solution (0.5 mg) and chalk suspension (DOX:chalk=1:1, 1:2, 1:5, 1:10, 1:15, and 1:20, mass ratio) were stirred in the dark for 12 h. The standard curve of DOX was shown in Fig. S1 (supplementary information). The drug efficiency reached 94.01% when the mass ratio of DOX to chalk was 1:10 and no longer increased, as observed in our previous research [39], and the drug-loading rate was 8.59%. Thus, this ratio was used in the subsequent experiments.

The pH of the normal human physiological environment is around 7.4, while the pH of the lysosome acidic environment is around 4.0–5.0 [47]. After nanocarriers achieve cell targeting, their antitumor effect can suffer from lysosome clearance. Therefore, stimuli-responsive nanomaterials have been designed to exhibit lysosomal escape ability to elevate drug efficacy [48, 49]. To explore the release profile of C-DOX@H22 CM in vitro, C-DOX@H22 CM was incubated in the PBS solution at pH 4.5 or pH 7.4. As shown in Fig. 1j, the release of C-DOX@H22 CM was markedly increased, with a cumulative release rate of higher than 60% after 4 h in the PBS solution at pH 4.5, while the cumulative release rate in the PBS solution at pH 7.4 was only 19.5% within 96 h. This pH-sensitive responsiveness of chalk not only prevents drug leakage but may also promote lysosomal membrane disruption to accelerate drug release under acidic conditions, which would contribute to excellent antitumor efficacy and fewer side effects.

As shown in Fig. 1k, the cytotoxicity test illustrated no noticeable killing effect on normal liver cells or cancer cells when incubated for 24 or 48 h. Furthermore, the blood compatibility of C-DOX@H22 CM was carefully monitored. There was almost no hemolysis appearance even with the treatment of C-DOX@H22 CM at 10 μg/mL (Fig. 1l), demonstrating the biosafety of these nanoparticles.

3.2 Cellular uptake of C-DOX@H22 CM

Due to the surface membrane proteins, cancer cell membrane-coated nanomaterials have become ideal drug delivery systems, conferring excellent immunocompatibility and homologous targeting abilities. The cellular uptake of C-DOX@H22 CM was first evaluated in RAW 264.7 cells. To study the immune escape capacity of C-DOX@H22 CM, RAW 264.7 cells were incubated with free DOX and C-DOX@H22 CM, and the fluorescence intensity was measured using flow cytometry. Compared to free DOX, as shown in Fig. 2a, the fluorescence intensity of C-DOX@H22 CM was lower ($P<$ 0.01). Various studies have shown that cancer cell membrane encapsulation significantly improves the stability of nanoparticles in the physiological environment and enhances cellular uptake in tumor cells through a homing effect compared to unencapsulated nanoparticles, therefore offering tremendous potential for their employment as individualized therapeutic agents in clinical oncology treatment [50].

Next, we measured the fluorescence intensity of C-DOX@ H22 CM in H22 tumor cells to confirm the homologous

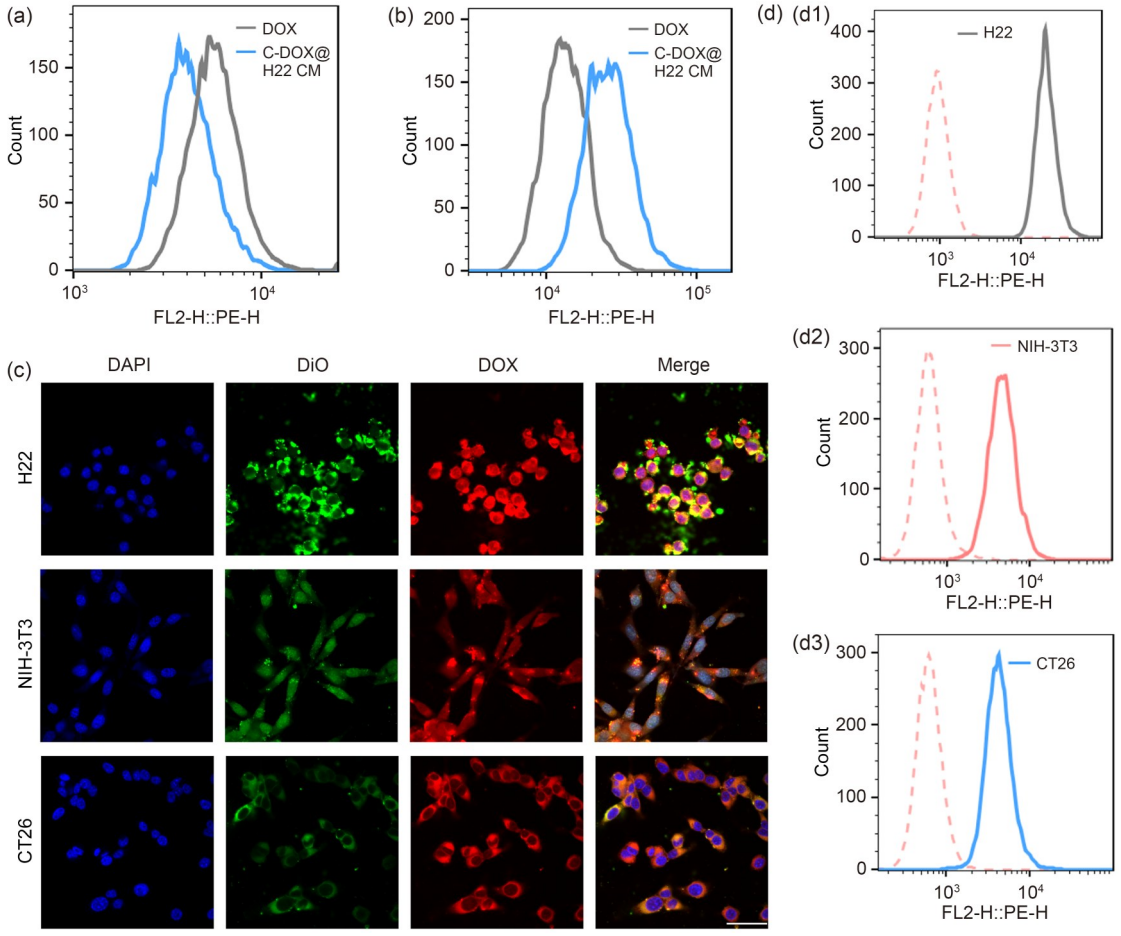

Fig. 2 Cellular uptake of C-DOX@H22 CM in vitro. The fluorescence intensity of C-DOX@H22 CM in RAW 264.7 cells (a) and H22 cells (b) by flow cytometry. (c) CLSM images of cellular uptake of C-DOX@H22 CM-DiO (assembled with DiO-labeled H22 cell membranes) by different cells. Scale bar: 50 μm. (d) Cellular uptake of C-DOX@H22 CM in different cell types by flow cytometry: (d1) H22; (d2) NIH-3T3; (d3) CT26

targeting ability of C-DOX@H22 CM. The fluorescence intensity of C-DOX@H22 CM was higher than that of free DOX (Fig. 2b). The internalization of C-DOX@H22 CM in different cells, such as H22, NIH-3T3, and CT26 cells, was also assessed. As expected, the homologous specificity of C-DOX@H22 CM was confirmed by the result of the strongest cellular uptake in H22 cells, while the uptake in normal cells, NIH-3T3, and CT26 colon tumor cells was weak with flow cytometry (Fig. 2d). In addition, we prepared C-DOX@H22 CM-DiO by assembling DiO-labeled H22 cell membranes with C-DOX to detect the fluorescence intensity under CLSM. As shown in Fig. 2c, the results of the CLSM were consistent with the flow cytometry experiment. Both NIH-3T3 and CT26 cells displayed only weak green and red fluorescent signals in the cytoplasm. In contrast, the strong yellow fluorescent signal (overlaid with green and red fluorescence) was observed in the cytoplasm of H22 cells, which might benefit from the expression of specific proteins on the cell membrane. In addition to the signal in the cytoplasm, a purple fluorescence signal (overlaid blue and red fluorescence) was observed in the cell nucleus. The cell membranes of different cell types contain unique lipids and proteins that largely determine the complex functions that the cells can perform. In particular, tumor cells have an innate ability to recognize and adhere to the source cancer cells with the aid of adhesion molecules on the cancer cell membranes, known as "Ho–Mo adhesion" [51–53]. These results indicated that C-DOX@H22 CM was more easily internalized by homologous cells and rapidly released DOX into the nucleus, which is conducive to the anti-cancer effect of HCC and has superior safety in normal cells to reduce side effects.

Moreover, C-DOX@RBCM was successfully prepared by coating with RBCMs to explore the selection of nanoparticles. The results demonstrated that C-DOX@ H22 CM exhibited better tumor targeting capability compared with the C-DOX@RBCM group (Fig. 3a). C-DOX@ H22 CM was further cocultured with H22 cells and NIH-3T3 normal cells to detect the homologous specificity under CLSM. As shown in Fig. 3b, the fluorescence intensity of C-DOX@ H22 CM in H22 cells was stronger than that in the other groups. However, the NIH-3T3 cells exhibited little drug fluorescence intensity in the two nanoparticle groups, while

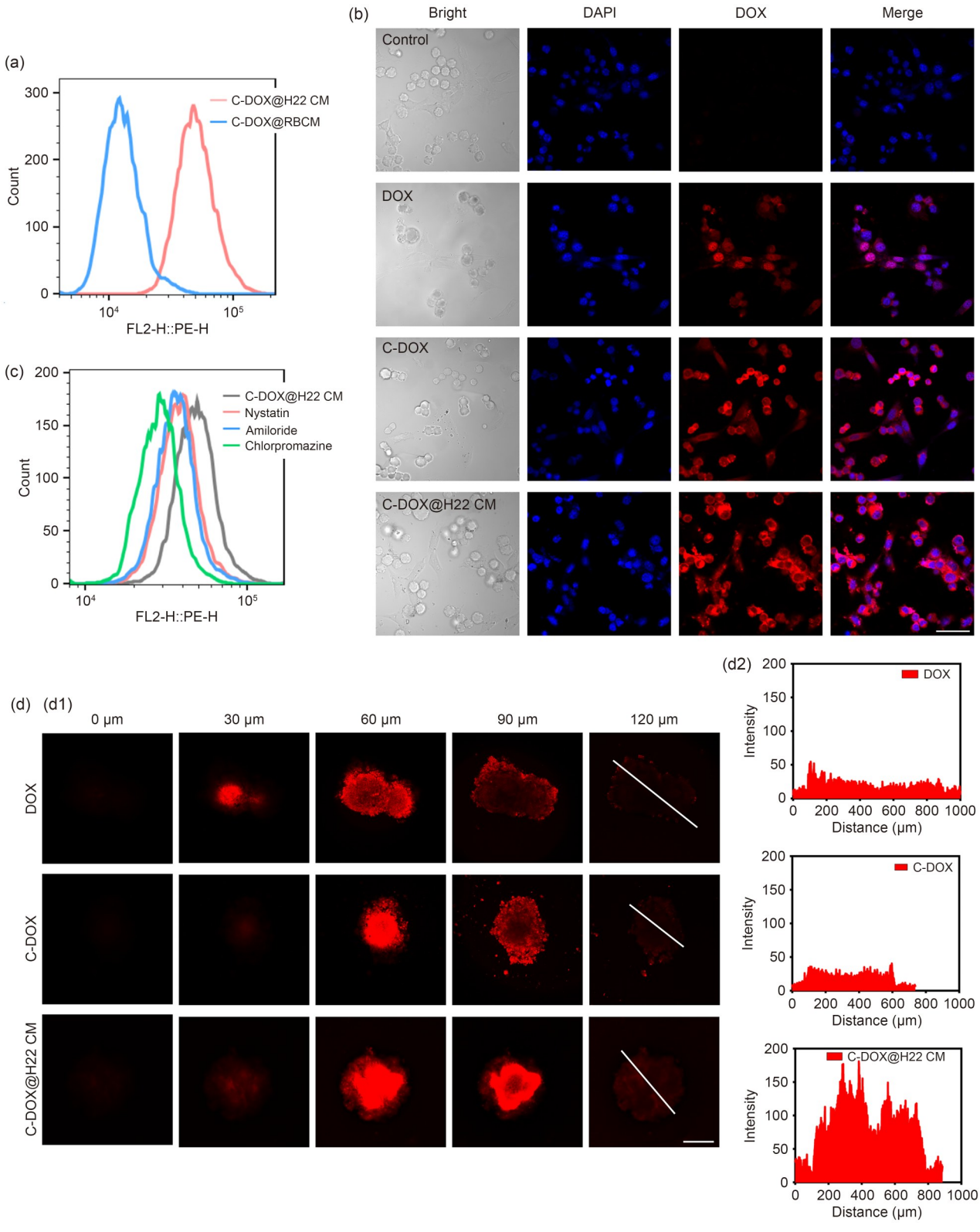

Fig. 3 Specific uptake and endocytic pathways of C-DOX@H22 CM. (a) Flow cytometry results of the mean fluorescence intensity of C-DOX@RBCM and C-DOX@H22 CM after H22 cell uptake. (b) CLSM images of H22 cells and NIH-3T3 normal cells incubated with C-DOX@H22 CM. Scale bar: 50 μm. (c) The effects of endocytosis inhibitors on the cellular uptake of C-DOX@H22 CM in H22 cells. After pretreatment with the three endocytosis inhibitors, H22 cells were cocultured with C-DOX@H22 CM, and then the cells were collected by flow cytometry to detect the fluorescent cellular uptake. (d) CLSM fluorescence images of H22 tumorspheres after the uptake of C-DOX@H22 CM (d1) and fluorescence intensity of C-DOX@H22 CM in a 120-μm cross-section of the tumorspheres (d2). Scale bar: 50 μm

the ratio of NIH-3T3 to H22 uptake significantly decreased after cell membrane coating, reflecting that the homologous cell membrane camouflaging could effectively enhance tumor targeting and diminish drug accumulation in normal cells. Collectively, the results confirmed the tumor homologous targeting ability and immune escape capacity of the biomimetic C-DOX@H22 CM drug delivery system.

The endocytic pathways of exogenous nanoparticles are mainly categorized into clathrin-mediated endocytosis (CME), caveolin-mediated endocytosis (CVME), lipid raft-mediated endocytosis, and macropinocytosis [54]. The endocytic process of C-DOX@H22 CM was evaluated. H22 cells were pretreated with three endocytic inhibitors, followed by C-DOX@H22 CM. Compared with the control group, as shown in Fig. 3c, the cellular uptake dramatically decreased in the chlorpromazine-pretreated group, indicating that the endocytosis of C-DOX@H22 CM was mainly dependent on the CME pathway. Pretreatment with nystatin and amiloride also inhibited the uptake of C-DOX@H22 CM, but both decreased less than that of the chlorpromazine-treated group, suggesting that a small portion of cellular uptake was partially mediated through CVME and macropinocytosis. In summary, the uptake of C-DOX@ H22 CM by H22 cells was carried out through CME, CVME, and macropinocytosis, but was more strongly reliant on the CME pathway.

To determine the penetration efficiency of C-DOX@H22 CM, a 3D tumorsphere system containing H22 and NIH-3T3 cells was developed. As expected, it was observed that the fluorescent signal of free DOX was located at the periphery of the tumorsphere (Fig. 3d), while the penetration depth of the nanoparticles increased after being wrapped by the cell membrane, of which the fluorescent signal on the cell membrane was closer to the core of the tumorsphere (reaching 120 μm), verifying that the cancer cell membrane coating could improve the permeability of the tumor.

3.3 Evaluation of the in vivo targeting capability and in vitro antitumor efficacy of C-DOX@H22 CM

The targeting efficiency of H22 cell membrane-coated NPs was examined in H22 tumor-bearing mice by ICG-labeled C@H22 CM. As shown in Fig. 4a, the C-ICG@ H22 CM group showed the strongest fluorescence signal in the tumor tissue at 6 h after injection compared with the free ICG, C-ICG, and C-ICG@RBCM groups. After 24 h of injection, the fluorescence intensity of the C-ICG@H22 CM group was mainly concentrated in the tumor but was also partially concentrated in the normal liver tissue. In particular, the fluorescence intensity of C-ICG@H22 CM was still higher

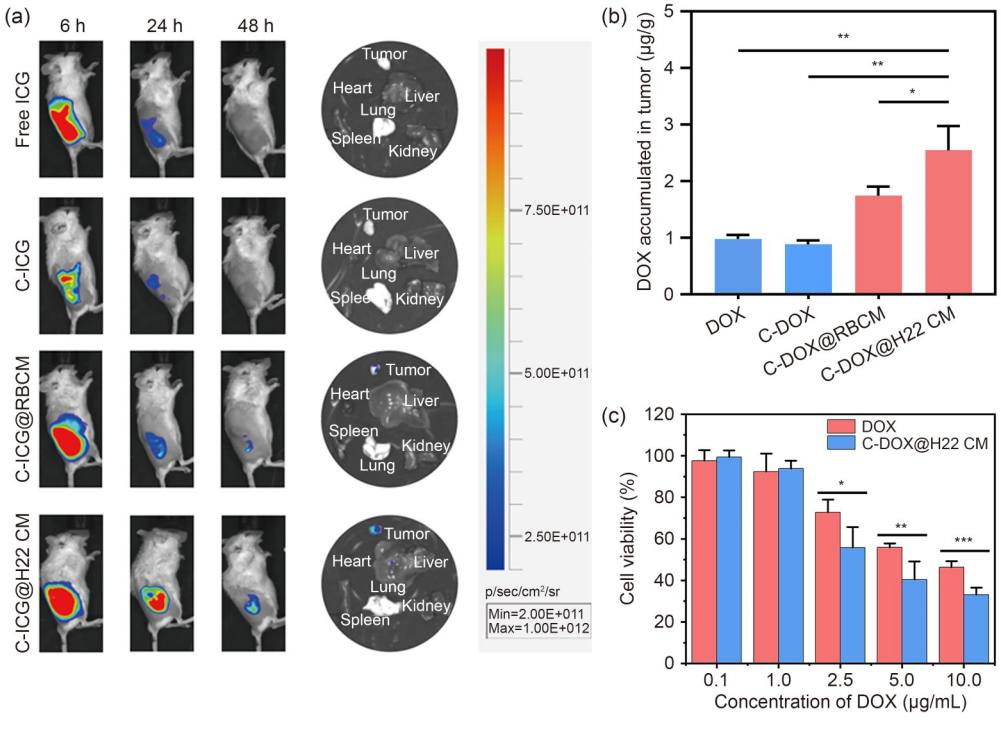

Fig. 4 Tumor targeting capability and in vitro antitumor efficacy of C-DOX@H22 CM. (a) Real-time fluorescence images of H22 tumor-bearing mice after intravenous injection of ICG-labeled nanoparticles at different time points and ex vivo fluorescence images of major tissues and tumors after 48 h intravenous injection of free ICG, C-ICG, C-ICG@RBCM, and C-ICG@H22 CM (n=3). (b) Quantitative analysis of tumor accumulation of DOX at 48 h postintravenous injection by fluorescence standard curve method (n=3). (c) Cell viability of H22 cells after incubation with C-DOX@H22 CM for 24 h at various concentrations of DOX (n=5). Data are expressed as mean±standard deviation. $^{*}P<0.05$, $^{**}P<0.01$, and $^{***}P<0.001$

than that of the C-ICG@RBCM group after 48 h of injection, while the fluorescence intensity in the tumor tissue of the free ICG and C-ICG groups basically disappeared, indicating that the homologous tumor cell membrane encapsulation improved the tumor targeting of the NPs. In addition, 48 h after the intravenous injections of free DOX, C-DOX, C-DOX@RBCM, and C-DOX@H22 CM, the mice were euthanized, and the tumors were harvested to measure the tumor accumulation of DOX via the fluorescence standard curve method (Fig. S3 in the supplementary information). As shown in Fig. 4b, the accumulation of DOX in the tumors of the C-DOX@H22 CM group was greater than that of the free DOX, C-DOX, and C-DOX@ RBCM groups. The accumulation of DOX was relatively weak in the tumors of the C-DOX@RBCM group and almost disappeared in the free DOX and C-DOX groups. This indicated that the homologous cell membrane coating could enhance the tumor-targeting capabilities of NPs and reduce the rapid clearance of free drugs and side effects.

Next, the in vitro antitumor effect of C-DOX@H22 CM on H22 cells was evaluated. H22 cells were treated with free DOX or C-DOX@H22 CM at DOX concentrations of 0.1, 1.0, 2.5, 5.0, and 10.0 μg/mL. As shown in Fig. 4c, the cytotoxicity of C-DOX@H22 CM was concentration-dependent. The cell viability of C-DOX@H22 CM was only (55.8±9.8)%, indicating more obvious cytotoxicity compared with the equivalent amount of DOX (P<0.05) at a low concentration of 2.5 μg/mL. These results demonstrated that C-DOX@H22 CM with a tumor cell membrane coating could enhance the antitumor effect of free DOX in vitro by promoting homologous drug targeting to HCC cancer cells, making it a potential candidate for antitumor therapy in vivo.

3.4 In vivo antitumor efficiency of C-DOX@H22 CM

The therapeutic ability of C-DOX@H22 CM was evaluated in an H22 cell-derived xenograft model. Figure 5a displays

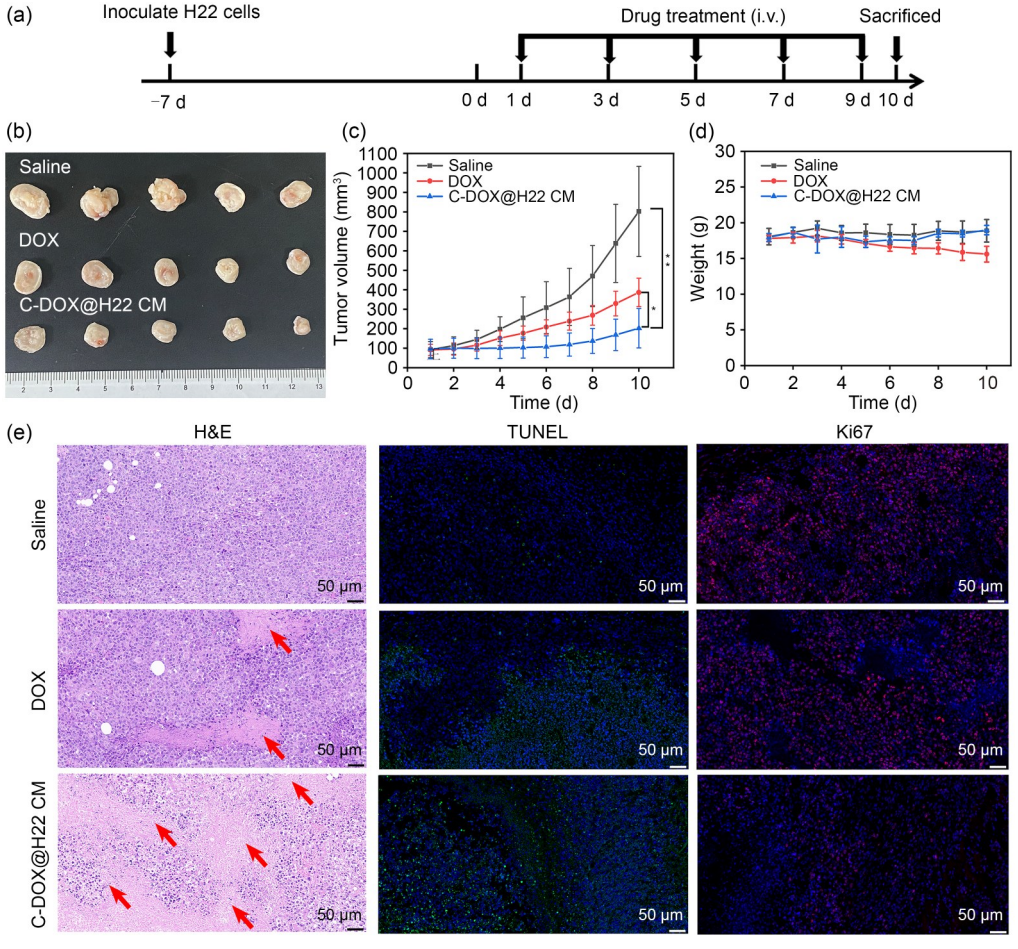

Fig. 5 Therapeutic effect of C-DOX@H22 CM in HCC subcutaneous tumor model. (a) Timeline of animal experiments in subcutaneous tumor mice. (b) Images of harvested tumors 9 d post-injection of saline, DOX, and C-DOX@H22 CM (n=5). Tumor volume curves (c) and body weight changes (d) of tumor-bearing mice treated with saline, DOX, and C-DOX@H22 CM (n=5). (e) H&E histological staining and immunofluorescence results of TUNEL and Ki67 of tumor tissues. The red arrows indicate apoptosis of tumor cells. Scale bar: 50 μm. Data are expressed as mean±standard deviation. $^{*}P$<0.05 and $^{**}P$<0.01

the timeline of the animal experiments in the subcutaneous tumor mice. Figure 5b shows that C-DOX@H22 CM could improve the antitumor effect. The tumor volume in the saline group was 3.96 times that in the C-DOX@H22 CM group; the tumor volume in the free DOX group was 1.91 times that in the C-DOX@H22 CM group. By recording the tumor size and body weight change of the mice, it was found that the HCC tumors' volume of C-DOX@H22 CM was significantly decreased compared with other groups, but there was no obvious weight loss compared with the free DOX group (Figs. 5c and 5d). Subsequently, the tumors were collected on the 10th day after four consecutive doses of C-DOX@H22 CM. As shown in Fig. 5e, the H&E staining section results of the tumor showed that the tumor necrosis and apoptosis of C-DOX@H22 CM-treated mice were more severe than that of the free DOX group. At the same time, the lower expression of Ki67 was observed at the periphery of tumor tissues in the C-DOX@H22 CM group, demonstrating that camouflaging with tumor cell membranes could effectively inhibit tumor growth; the TUNEL immunofluorescence results supported this conclusion. As a result, the bio-designed tumor cell membrane with chalk coating showed superior antitumor efficacy against HCC.

3.5 In vivo safety evaluation

We assessed the biocompatibility of C-DOX@H22 CM during tumor treatment. The heart, liver, spleen, lung, and kidney were collected after four consecutive injections for H&E staining. The C-DOX@H22 CM conferred no obvious damage to normal organs compared with the saline groups (Fig. 6c). Besides, the blood was obtained to analyze the physical health indicators of the mice. No apparent difference was found in the blood routine and liver function between the DOX@H22 CM and saline groups, indicating the biosafety of C-DOX@H22 CM (Figs. 6a and 6b). Taken together,

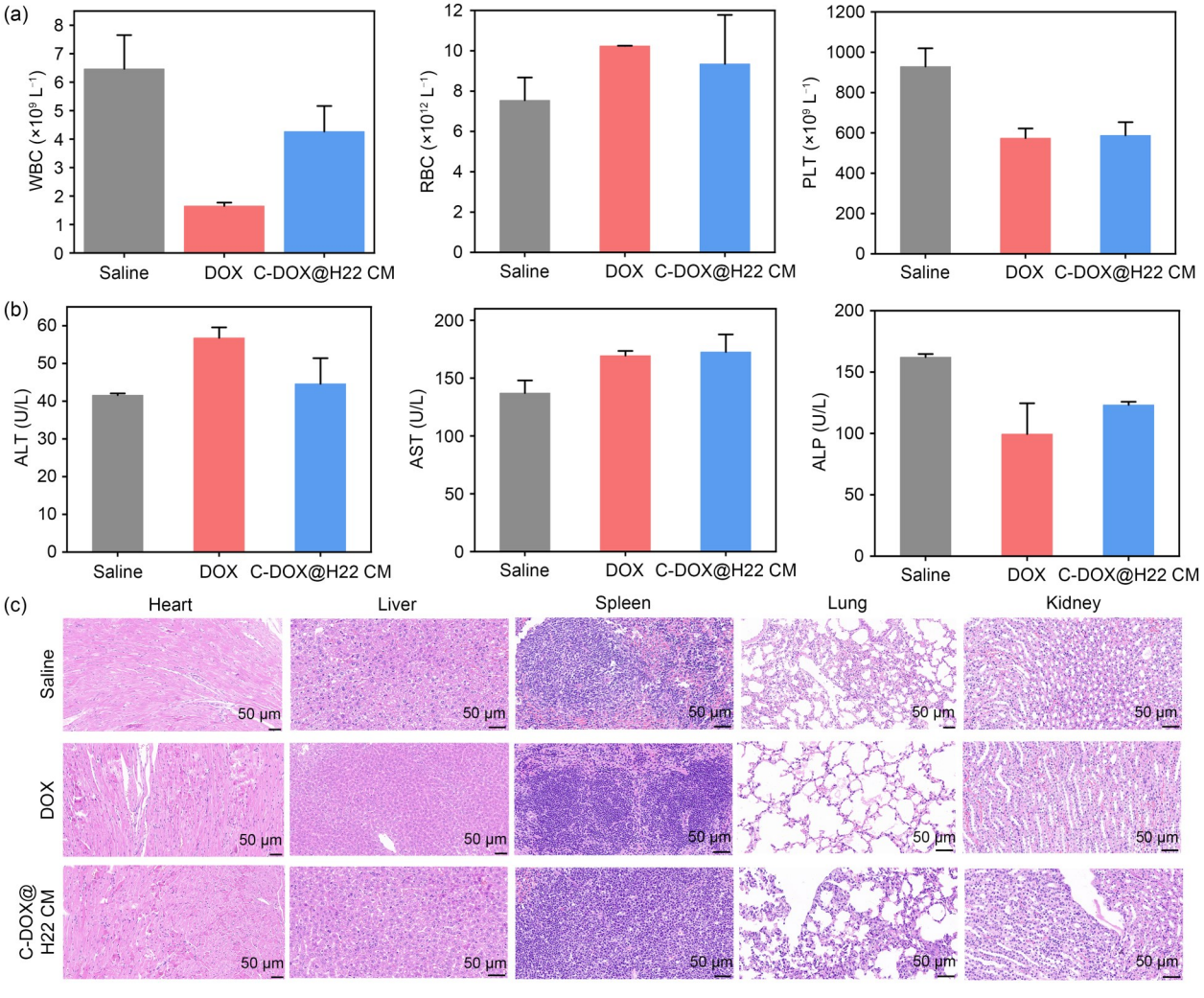

Fig. 6 In vivo biosafety evaluations of C-DOX@H22 CM therapy. Blood routine examination (a) and liver function analysis (b) of tumor-bearing mice after treatment with saline, DOX, and C-DOX@H22 CM (n=3). (c) H&E histological staining of the heart, liver, spleen, lung, and kidney from mice from the saline, DOX, and C-DOX@H22 CM treatment groups. Scale bar: 50 μm. Data are expressed as mean±standard deviation

these results indicate that C-DOX@H22 CM has excellent biosafety in vivo with minimal side effects.

4 Conclusions

In this study, we prepared a cancer cell membrane-camouflaged pH-sensitive natural chalk delivery system for the treatment of HCC. Compared with RBCM-coated or non-cell-membrane-coated nanoparticles, this biomimetic nanoparticle (C-DOX@H22 CM) can significantly improve the immune escape and homologous targeting properties, thereby enhancing drug accumulation. Furthermore, C-DOX@H22 CM efficiently entered HCC cells mainly through CME and exhibited pH-sensitive drug release. More interestingly, the in vitro experiments demonstrated that C-DOX@H22 CM possessed deep penetration properties and therapeutic effects without obvious biotoxicity. Importantly, the good antitumor efficacy and biosafety of C-DOX@H22 CM were also demonstrated in the H22 tumor-bearing mouse model, which suggested its great potential for clinical translation.

Supplementary Information The online version contains supplementary material available at https://doi.org/10.1631/bdm.2400341.

Acknowledgements The article was supported by Zhejiang Medical Science and Technology Project (No. 2023KY704), Zhejiang Traditional Chinese Medicine Science and Technology Project (Nos. 2023ZR107 and 2024ZF094), Special Research Fund for Hospital Pharmacy of Zhejiang Pharmaceutical Association (No. 2021ZYY08), and Zhejiang Medical Association Clinical Research Fund (Nos. 2021ZYC-A64 and 2021ZYC-A67).

Author contributions YBZ performed the experiments and wrote the manuscript. PFC collected and analyzed the data. LJZ conducted the data analysis. QL revised the manuscript. JYQ conceived the study, reviewed the draft, and provided financial support. All authors read and approved the final manuscript.

Declarations

Conflict of interest The authors declare that they have no conflict of interest.

Ethical approval The animal experiments were approved by the Institutional Animal Care and Use Committee (IACUC) of the First Affiliated Hospital, Zhejiang University School of Medicine, China (Approval No. 20231291).

Data availability The data that support the findings of this study are available from the corresponding authors upon reasonable request.

References

1. Bray F, Laversanne M, Sung H et al (2024) Global cancer statistics 2022: GLOBOCAN estimates of incidence and mortality worldwide for 36 cancers in 185 countries. CA Cancer J Clin 74(3):229–263. https://doi.org/10.3322/caac.21834
2. Fan J, Yang GS, Fu ZR et al (2009) Liver transplantation outcomes in 1078 hepatocellular carcinoma patients: a multi-center experience in Shanghai, China. J Cancer Res Clin Oncol 135(10): 1403–1412. https://doi.org/10.1007/s00432-009-0584-6
3. Huang ZM, Han X, Wang J et al (2024) A prospective, single-arm, phase 2 study of modified transarterial chemoembolization using low-dose chemotherapy with blank microspheres plus low-dose lenvatinib and microwave ablation in patients with large (⩾7 cm) unresectable hepatocellular carcinoma: the TALEM trial. Liver Cancer 13(4):438–450. https://doi.org/10.1159/000536518
4. Huang ZK, Chen TJ, Li WB et al (2024) Atezolizumab and bevacizumab plus transarterial chemoembolization and hepatic arterial infusion chemotherapy for patients with high tumor burden unresectable hepatocellular carcinoma: a multi-center cohort study. Int Immunopharmacol 139:112711. https://doi.org/10.1016/j.intimp.2024.112711
5. Yu QY, Gao Y, Dai WC et al (2024) Cell membrane-camouflaged chitosan-polypyrrole nanogels co-deliver drug and gene for targeted chemotherapy and bone metastasis inhibition of prostate cancer. Adv Healthc Mater 13(20):e2400114. https://doi.org/10.1002/adhm.202400114
6. Zhang YJ, Wang Y, Zhu AN et al (2024) Dual-targeting biomimetic semiconducting polymer nanocomposites for amplified theranostics of bone metastasis. Angew Chem Int Ed 63(2): e202310252. https://doi.org/10.1002/anie.202310252
7. Xin C, Xia N, Zhang L (2024) Light-based 3D printing of stimulus-responsive hydrogels for miniature devices: recent progress and perspective. Bio-Des Manuf 7(4):721–746. https://doi.org/10.1007/s42242-024-00295-1
8. Liu S, Zhang X, Bai Z et al (2024) Light/pH dual controlled drug release "nanocontainer" alleviates tumor hypoxia for synergistic enhanced chemotherapy, photodynamic therapy and chemodynamic therapy. Bio-Des Manuf 7(6):955–971. https://doi.org/10.1007/s42242-024-00310-5
9. Liu HN, Pan D, Yao ZY et al (2024) Efficacy and safety of gemcitabine/nab-paclitaxel combined with anlotinib and PD-1 inhibitors as a first-line treatment for advanced pancreatic cancer. Int Immunopharmacol 139:112635. https://doi.org/10.1016/j.intimp.2024.112635
10. Rubio MJ, Manzano A, de Sande LM et al (2024) Retrospective multicenter study of elderly patients with platinum-sensitive relapsed ovarian cancer treated with trabectedin and pegylated liposomal doxorubicin (pld) in a real-world setting: a geico study. BMC Cancer 24(1):803. https://doi.org/10.1186/s12885-024-12577-z
11. Wang P, Wang YF, Li HM et al (2024) A homologous-targeting cGAS-STING agonist multimodally activates dendritic cells for enhanced cancer immunotherapy. Acta Biomater 177:400–413. https://doi.org/10.1016/j.actbio.2024.02.003
12. Kuperkar K, Atanase LI, Bahadur A et al (2024) Degradable polymeric bio(nano)materials and their biomedical applications: a comprehensive overview and recent updates. Polymers 16(2):206. https://doi.org/10.3390/polym16020206
13. Gabizon A, Horowitz AT, Goren D et al (2003) In vivo fate of folate-targeted polyethylene-glycol liposomes in tumor-bearing mice. Clin Cancer Res 9(17):6551–6559
14. Huang TY, Guo YQ, Wang ZQ et al (2024) Biomimetic dual-target theranostic nanovaccine enables magnetic resonance imaging and chemo/chemodynamic/immune therapy of glioma. ACS Appl Mater Interfaces 16(21):27187–27201. https://doi.org/10.1021/acsami.4c05831
15. Wang Y, Wang JL, Ye RM et al (2024) Cancer cell-mimicking

Prussian blue nanoplatform for synergistic mild photothermal/chemotherapy via heat shock protein inhibition. ACS Appl Mater Interfaces. https://doi.org/10.1021/acsami.4c00873
16. Feng X, Brown CM, Wang HD et al (2024) Carrier-free chemophototherapeutic nanomedicines with endo/lysosomal escape function enhance the therapeutic effect of drug molecules in tumors. J Mater Chem B 12(27):6703–6715. https://doi.org/10.1039/D4TB00465E
17. Liu ZM, Zhou XF, Li Q et al (2023) Macrophage-evading and tumor-specific apoptosis inducing nanoparticles for targeted cancer therapy. Acta Pharm Sin B 13(1):327–343. https://doi.org/10.1016/j.apsb.2022.05.010
18. Jiang Q, Wang K, Zhang XY et al (2020) Platelet membrane-camouflaged magnetic nanoparticles for ferroptosis-enhanced cancer immunotherapy. Small 16(22):2001704. https://doi.org/10.1002/smll.202001704
19. Song YZ, Shou X, Sheng B et al (2023) Cell membranes from tumor-tropic MSCs screened by a microfluidic chip for drug nanoparticles encapsulation and cancer targeted therapy. Adv Healthc Mater 12(17):2202904. https://doi.org/10.1002/adhm.202202904
20. Wang YZ, Zhang C, Han SY et al (2024) Cancer cell membrane camouflaged biomimetic gelatin-based nanogel for tumor inhibition. Chin Chem Lett 35(11):109578. https://doi.org/10.1016/j.cclet.2024.109578
21. Wang DD, Yao YZ, Xiao Y et al (2021) Ultrasound responsive erythrocyte membrane-derived hybrid nanovesicles with controlled drug release for tumor therapy. Nanoscale 13(22):9945–9951. https://doi.org/10.1039/D1NR01916C
22. Meng ZJ, Wang TT, Hu YX et al (2024) Macrophage membrane-camouflaged aggregation-induced emission nanoparticles enhance photodynamic-immunotherapy to delay postoperative tumor recurrence. Adv Healthc Mater 13(4):2302156. https://doi.org/10.1002/adhm.202302156
23. Ye JM, Fan YY, She YG et al (2024) Biomimetic self-propelled asymmetric nanomotors for cascade-targeted treatment of neurological inflammation. Adv Sci 11(22):2310211. https://doi.org/10.1002/advs.202310211
24. Li RY, Fu DX, Yuan X et al (2024) Oral heterojunction coupling interventional optical fiber mediates synergistic therapy for orthotopic rectal cancer. Small 20(43):2404741. https://doi.org/10.1002/smll.202404741
25. Fan YY, Ye JM, Kang Y et al (2024) Biomimetic piezoelectric nanomaterial-modified oral microrobots for targeted catalytic and immunotherapy of colorectal cancer. Sci Adv 10(19):eadm9561. https://doi.org/10.1126/sciadv.adm9561
26. Ye JM, Fan YY, Kang Y et al (2025) Biomimetic dual-driven heterojunction nanomotors for targeted catalytic immunotherapy of glioblastoma. Adv Funct Materials 35(9):2416265. https://doi.org/10.1002/adfm.202416265
27. Kong N, Zhang HJ, Feng C et al (2021) Arsenene-mediated multiple independently targeted reactive oxygen species burst for cancer therapy. Nat Commun 12(1):4777. https://doi.org/10.1038/s41467-021-24961-5
28. Niu GL, Bi XQ, Kang Y et al (2024) An acceptor–donor–acceptor structured nano-aggregate for NIR-triggered interventional photoimmunotherapy of cervical cancer. Adv Mater 36(39):2407199. https://doi.org/10.1002/adma.202407199
29. Cui HQ, Zhang XY, Zhang ZZ et al (2023) Killing three birds with one stone: tumor-membrane-decorated Prussian blue nanovaccines for synergistic management of skin tumors, radiation dermatitis and wounds. Compos Part B Eng 264:110900. https://doi.org/10.1016/j.compositesb.2023.110900
30. Chen YL, Zhi SY, Ou JX et al (2023) Cancer cell membrane-coated nanoparticle co-loaded with photosensitizer and toll-like receptor 7 agonist for the enhancement of combined tumor immunotherapy. ACS Nano 17(17):16620–16632. https://doi.org/10.1021/acsnano.3c02724
31. Li SL, Jiang SS, Rahman MSU et al (2023) Pre-induced ICD membrane-coated carrier-free nanoparticles for the personalized lung cancer immunotherapy. Small Meth 7(5):2201569. https://doi.org/10.1002/smtd.202201569
32. Gao YH, Wang ZY, Jin XM et al (2024) Enhanced osteosarcoma immunotherapy via $CaCO_3$ nanoparticles: remodeling tumor acidic and immune microenvironment for photodynamic therapy. Adv Healthc Mater 13(23):2400538. https://doi.org/10.1002/adhm.202400538
33. Martins SA, Costa RR, Brito A et al (2024) Multifunctional calcium-based nanocarriers for synergistic treatment of triple-negative breast cancer. J Colloid Interface Sci 674:500–512. https://doi.org/10.1016/j.jcis.2024.06.159
34. Zhao F, Wang C, Wang H et al (2024) Acidity-responsive Fe-PDA@$CaCO_3$ nanoparticles for photothermal-enhanced calcium-overload- and reactive-oxygen-species-mediated tumor therapy. ACS Appl Mater Interfaces 16(33):43364–43373. https://doi.org/10.1021/acsami.4c09143
35. Fang TX, Cao XN, Wang L et al (2024) Bioresponsive and immunotherapeutic nanomaterials to remodel tumor microenvironment for enhanced immune checkpoint blockade. Bioact Mater 32:530–542. https://doi.org/10.1016/j.bioactmat.2023.10.023
36. Zhang CX, Li SH, Yu A et al (2019) Nano $CaCO_3$ lysosomal bombs enhance chemotherapy drug efficacy via rebalancing tumor intracellular pH. ACS Biomater Sci Eng 5(7):3398–3408. https://doi.org/10.1021/acsbiomaterials.9b00436
37. Liu H, Wen ZY, Liu ZH et al (2024) Unlocking the potential of amorphous calcium carbonate: a star ascending in the realm of biomedical application. Acta Pharm Sin B 14(2):602–622. https://doi.org/10.1016/j.apsb.2023.08.027
38. Okhrimenko DV, Dalby KN, Skovbjerg LL et al (2014) The surface reactivity of chalk (biogenic calcite) with hydrophilic and hydrophobic functional groups. Geochim Cosmochim Acta 128:212–224. https://doi.org/10.1016/j.gca.2013.12.011
39. Li J, Ma LP, Wang C et al (2022) Rationally designed oral DOX gels for colon-specific administration. Gels 8(12):759. https://doi.org/10.3390/gels8120759
40. Wu KX, He M, Mao BL et al (2024) Enhanced delivery of CRISPR/Cas9 system based on biomimetic nanoparticles for hepatitis B virus therapy. J Control Release 374:293–311. https://doi.org/10.1016/j.jconrel.2024.08.019
41. Ying KK, Zhu YF, Wan JQ et al (2023) Macrophage membrane-biomimetic adhesive polycaprolactone nanocamptothecin for improving cancer-targeting efficiency and impairing metastasis. Bioact Mater 20:449–462. https://doi.org/10.1016/j.bioactmat.2022.06.013
42. Ren XL, He LB, Tian XH et al (2019) pH and folic acid dual responsive polysaccharide nanospheres used for nuclear targeted cancer chemotherapy. Colloids Surf B Biointerfaces 178:445–451. https://doi.org/10.1016/j.colsurfb.2019.03.028
43. Shi WG, Ma ZQ, Wang YL et al (2017) HPAM assisted controllable synthesis of peanut-like $CaCO_3$ in fixed silicate solution. Colloids Surf A Physicochem Eng Aspects 535:34–40. https://doi.org/10.1016/j.colsurfa.2017.09.031
44. Li J, Wang XD, Zheng DY et al (2018) Cancer cell membrane-coated magnetic nanoparticles for MR/NIR fluorescence dual-modal imaging and photodynamic therapy. Biomater Sci 6(7):1834–1845. https://doi.org/10.1039/C8BM00343B

45. Wang YM, Wang D, Zhang YY et al (2023) Tumor microenvironment-adaptive nanoplatform synergistically enhances cascaded chemodynamic therapy. Bioact Mater 22:239–253. https://doi.org/10.1016/j.bioactmat.2022.09.025
46. Liu XJ, Sun YX, Xu SS et al (2019) Homotypic cell membrane-cloaked biomimetic nanocarrier for the targeted chemotherapy of hepatocellular carcinoma. Theranostics 9(20):5828–5838. https://doi.org/10.7150/thno.34837
47. Gao Y, Jia L, Wang Q et al (2019) pH/Redox dual-responsive polyplex with effective endosomal escape for codelivery of siRNA and doxorubicin against drug-resistant cancer cells. ACS Appl Mater Interfaces 11(18):16296–16310. https://doi.org/10.1021/acsami.9b02016
48. Chen PW, Yang WQ, Hong T et al (2022) Nanocarriers escaping from hyperacidified endo/lysosomes in cancer cells allow tumor-targeted intracellular delivery of antibodies to therapeutically inhibit c-MYC. Biomaterials 288:121748. https://doi.org/10.1016/j.biomaterials.2022.121748
49. Xue XL, Qian CG, Fang HB et al (2019) Photoactivated lysosomal escape of a monofunctional Pt^{II} complex Pt-BDPA for nucleus access. Angew Chem Int Ed 58(36):12661–12666. https://doi.org/10.1002/anie.201906203
50. Li XC, Lin YL, Yang Z et al (2023) Cancer cell membrane biomimetic nanosystem for homologous targeted dual-mode imaging and combined therapy. J Colloid Interface Sci 652:770–779. https://doi.org/10.1016/j.jcis.2023.08.109
51. Wang YQ, Qiu YZ, Chen SH et al (2023) Functionalized tumor cell membrane-camouflaged photo-activatable nanoparticle for spatiotemporal antitumor therapy. Chem Eng J 474:145676. https://doi.org/10.1016/j.cej.2023.145676
52. Guo H, Li X, Mao DX et al (2024) Homologous-magnetic dual-targeted metal-organic framework to improve the Anti-hepatocellular carcinoma efficacy of PD-1 inhibitor. J Nanobiotechnol 22(1):206. https://doi.org/10.1186/s12951-024-02469-6
53. Fang RH, Hu CMJ, Luk BT et al (2014) Cancer cell membrane-coated nanoparticles for anticancer vaccination and drug delivery. Nano Lett 14(4):2181–2188. https://doi.org/10.1021/nl500618u
54. Huang SN, Song CZ, Miao JX et al (2023) Red blood cell membrane-coated functionalized Au nanocage as a biomimetic platform for improved microRNA delivery in hepatocellular carcinoma. Int J Pharm 642:123044. https://doi.org/10.1016/j.ijpharm.2023.123044